Cooperative Minimum Expected Length Planning for Robot Formations in Stochastic Maps

Pablo Urcola, María T. Lázaro, José A. Castellanos and Luis Montano*

Instituto de Investigación en Ingeniería de Aragón. Universidad de Zaragoza. c/ Mariano Esquillor s/n. 50018. Zaragoza. Spain.

Abstract

This paper addresses a tightly integrated multi-robot planning, localization and navigation system in stochastic scenarios. We present a novel motion planning technique for robot formations in such kinds of environments, which computes the most likely global path in terms of a defined minimum expected length (EL). EL evaluates the expected cost of a path considering the probability of finding a non traversable zone and the cost of using an alternative traversable path. A local real time re-planning technique based on the probabilistic model is also developed for the formation when the scenario changes. The formation adapts its configuration to the shape of the free room. The partial views of all the robots are integrated to update the multi-robot localization using a modified EKF based on the measurement differencing technique which improves estimation consistency. As a result, a lower uncertainty map of the local navigation area is obtained for re-planning purposes. Experimental results, both in simulation and in real office-like settings, illustrate the performance of the described approach where a hybrid, centralized-distributed, architecture with wireless communication capabilities is used.

Keywords: Planning under uncertainty, Stochastic maps, Cooperative formations localization and navigation, Hybrid architecture

1. Introduction

The interest in the design, development and implementation of multi-vehicle systems has grown tremendously both in the fields of robotics and control systems technology due to their enhanced reliability and robustness over single-vehicle systems.

Key applications such as factory automation, surveillance, exploration or rescue missions may benefit from the use of geometrically constrained multi-robot systems, known as *robot formations* where close cooperation and coordination among the, possibly heterogeneous, vehicles of the team is mandatory for the successful joint mission completion. For instance, the formation can be used to escort a group of people to the exit of a building in an emergency situation where the robots in the formation structure delimit a safe area for them and are spatially arranged to provide a broader field of view to the system.

During the execution of the mission, formation control, either centralized or distributed, keeps the team members on rigid predefined relative positions whilst moving towards the goal. A well-known approach to multi-robot coordination [1] is the leader-following approach where the robot followers navigate coordinately as commanded by the robot leader to reach the mission objectives, whilst maintaining a certain geometric shape (e.g., equilateral triangle, regular pentagon, etc), previously imposed to the formation. However, realistic scenarios with cluttered and dynamic obstacles prevent the formation from moving in the predefined shape along all its trajectory to the goal and thus the shape of the formation must be temporarily adapted to the environment.

The adaptability in the formation shape required to overcome the cluttered zones can be achieved by modeling the links between the robots as virtual spring-damper systems [2, 3]. Furthermore, this approach offers an important advantage when addressing the formation path planning problem, solved only by the robot

*Corresponding author

Email address: urcola@unizar.es, mtlazaro@unizar.es, jacaste@unizar.es, montano@unizar.es (Pablo Urcola, María T. Lázaro, José A. Castellanos and Luis Montano)

leader, in contrast to approaches based on virtual structures [4] where paths must be computed for all team members and imply additional computational efforts to adapt their trajectories to unexpected obstacles in the environment.

In [5], the authors propose a method for planning trajectories for formations of robots under uncertainty using potential fields and a fast marching algorithm to find the optimal solution. However, the uncertainty is only applied on the relative localization of the robots with respect to the others rather than to the obstacles in the map.

The localization of a robot formation can be formulated in the general setting of multi-robot localization, where several approaches have been reported in the literature using inter-robot measurements (e.g., in absence of previous knowledge about the navigation area [6, 7, 8]), landmark observations (e.g., in presence of a grid-based [9] or feature-based map [10]) or even both of them [11]. Interestingly, EKF-based distributed approaches using inter-robot measurements aimed at real-time performance have been reported [12, 13].

During the world modeling phase, uncertainty derived from noisy sensors is incorporated into the maps used later for path planning. Thus, the algorithms applied in deterministic scenarios to compute the best paths for the robots, such as those collected in [14], are no longer valid. For path planning, it is common to assume that the state of the robot is well known and that the actions are deterministic, as opposed to the POMDP approaches for robot control. This assumption is crucial because motion or localization uncertainty makes mandatory to minimize the risk of getting lost. There are mathematically sound suboptimal planning under motion and localization uncertainty methods such as [15], using POMDPs, or [16] and [17], planning in the belief space. These solutions are, thus, finding the paths that minimizes the uncertainty of the robot localization at the goal position.

However, assuming that motion and localization are always reliable, minimizing the position uncertainty is no longer an issue. Instead, it is incorporated into the knowledge of the connectivity or traversability of the environment. This lack of deterministic information implies that only the expectation of the length of a path can be computed, based on the prior and on the observations that the robots will perform during the mission. In [18], the authors propose a graph-based algorithm to compute the expected shortest path, making the markovian assumption that the connectivity of the scenario may eventually change during the execution of the mission. Some approaches like [19], make use of the graphs created during the map-building phase to compute minimum uncertainty paths to the goal. However, even though the authors extend the graph to cover trajectories not performed during the map-building, these additional elements added do not consider the presence of obstacles. Moreover, the new potential trajectories added, as they are further away from the features in the map, present higher uncertainty levels than those trajectories used to build the map. Thus, looking for the minimum uncertainty path will never select one of those added paths.

In this work we propose a global path planning – local replanning scheme that assumes a static scenario for global path planning but that is able to deal with changes locally.

From a system architecture view point, the performance of robot formations during mission execution can be described in terms of modularity and scalability of the underlying probabilistic framework and software components, thus favoring distributed or decentralized approaches. However, from the perspective of precision, reliability and robustness, the close cooperation among the different vehicles of the robot formation, in a centralized framework, would result in a jointly coherent understanding of the navigation environment, thus reducing the uncertainty both during the localization, e.g., wider and integrated fields of view, and path planning, e.g., due to alternative paths reachable by robot followers. Therefore, a hybrid centralized-distributed approach to trade-off the advantages of both perspectives without compromising the success of the commanded mission can be the best choice at hand.

The work presented in this paper develops new techniques for global and local path planning, and extends previous work reported by the authors in localization of multi-robot systems in stochastic maps [10] and motion control for robot formations [20], which are tightly integrated in the whole system to obtain the maximum benefits from their interaction. The main contributions of the work are: (i) a global path planning that minimizes the expected length in a stochastic map; (ii) a cooperative sensor-based local re-planning in the stochastic map; (iii) a multi-vehicle consistent localization (robot pose tracking) in stochastic maps built from the multiple views of the robots; (iv) a hybrid centralized-distributed architecture, using real-time wireless communication. The robot leader centralizes the information and executes the global processes, whilst navigation of the follower robots is distributed and executed by them. Experimental results, both in simulation and in real office-like settings, illustrate the performance of each of the techniques developed and of the whole system.

The rest of this paper is organized as follows: section 2 presents robot formations from the perspective of the leader-following approach, where a dynamical model based on the virtual spring-damper analogy is used; section 3 introduces the concepts of traversability maps and minimum expected length paths in a generic graph-based framework; in section 4 this concept is applied to obtain global minimum expected length paths from a global traversability map derived from a featured-based stochastic map; section 5 describes pose tracking and cooperative local path planning and navigation for the robot formation in dynamic scenarios; section 6 reports both simulated and real experiments obtained by a robot formation in the presence of sensing, localization and mapping uncertainties as described throughout the paper; finally, section 7 elaborates on the conclusions of the reported work and suggests continuation lines for the near future.

2. Probabilistic Robot Formations

We consider formations made up of $r+1$ robots where the leader R_0 is virtually linked to each of the followers $R_1, \ldots, R_r$. Each link is composed by two spring-damper systems: one is in charge of maintaining the distance among the robots and the other controls the relative angle. These links induce virtual forces on the robots, producing their movements, as shown in Fig. 1.

Let the location of the formation be represented by a discrete-time stochastic state vector $\mathbf{x}_{\mathcal{R}} = [\mathbf{x}_{R_0}^{B}, \mathbf{x}_{R_1}^{R_0}, \cdots, \mathbf{x}_{R_j}^{R_0}, \cdots, \mathbf{x}_{R_r}^{R_0}]^T$ formed by the location of the robot leader R_0 with respect to (wrt) a base reference frame B and the location of each robot follower R_j wrt the robot leader R_0. This leader-centric representation reduces the volume of uncertainty for the state vector $\mathbf{x}_{\mathcal{R}_k}$, in comparison with an absolute representation wrt the base frame B of each robot location vector and, therefore, linearization errors due to large uncertainty values are minimized [21]. Thus, a dynamic model of the robot formation is given by,

$$\mathbf{x}_{\mathcal{R}_k} = \mathbf{f}(\mathbf{x}_{\mathcal{R}_{k-1}}, \mathbf{F}_{\mathcal{R}_{k-1}}) + \mathbf{v}_{k-1} \tag{1}$$

where, $\mathbf{F}_{\mathcal{R}_{k-1}} = \{\mathbf{F}_0, \mathbf{F}_1, \ldots, \mathbf{F}_r\}$, the set of virtual forces acting on each of the vehicles of the robot formation, are transformed into linear and rotational velocity commands for each non-holonomic vehicle using a differential-drive model [22], and $\mathbf{v}_{k-1}$ represents a zero-mean white noise sequence with a block-diagonal covariance matrix $\mathbf{Q}_{k-1}$. Note that each of the virtual forces $\mathbf{F}_j$ acting on vehicle R_j is not directly the force

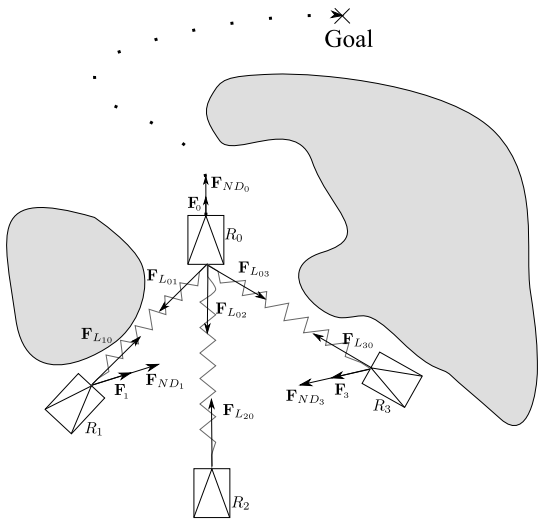

Figure 1: Simplified representation of the virtual spring-damper analogy for formation control in a cluttered environment where only linear springs are represented. In this example, the robot formation is formed by a robot leader R_0, and three robot followers R_1, R_2 and R_3. Virtual forces acting on each vehicle drive the robot formation towards the goal destination whilst adapting the geometric structure to the cluttered environment and avoiding obstacles and dynamic objects along the way.

generated by the link between robots. It is a combination of the link force $F_{L_{j0}}$ and an obstacle avoidance force $\mathbf{F}_{ND_j}$, as proposed by [20]. Additionally, the leader R_0 experiences the attraction force of the next way-point along its planned trajectory towards the goal destination.

3. Path Planning in Traversability Maps

Path planning for robot formations can be stated globally for all the robots of the team. But that approach has a high computational burden. In this work, we propose a flexible alternative approach, computationally lighter. The path planning is achieved by the leader of the formation, and the followers maintain the formation adapting to the environment by means of a spring-damper analogy (see more details in [3]). The formation is maintained while possible, otherwise it adapts its shape to the scenario structure. In the worst case, the formation will become a chain, so the path planned by the leader will also be feasible for the followers.

In this paper, we consider the path planning problem using a graph model based on the ones proposed in [18] and [23]. The scenario is modeled as a graph $G = (V, E)$, named in advance *traversability map*, where the vertices V are locations in the scenario and the edges E represent the connectivity between pairs of vertices. Each edge

that connects two vertices (u, v) is labeled with $L(u, v)$ the distance between the vertices and with $P(u, v)$ the probability for the edge to be traversable. During the execution of the mission, the actual state of the edges (traversable or not) is observable and thus, this information can be incorporated into the path planning algorithm to obtain the optimal path. This formulation of the path planning problem fits the Canadian traveller problem [24], which was first stated by [25] but is still not solved.

It is worth remarking that the optimal path computed with prior information may not be traversable during the execution and an alternative path to the goal may be required. The desired path is the one that minimizes the expected distance to reach the goal, including the cases when the initial path is not traversable and another path must be used. The idea behind this expected length of a path is that it may be worth to explore a possibly very short path to the goal but only if there is an alternative path good enough in case the original path is not traversable.

In [18] the authors assume that the graph is not static and thus the state of the edges might eventually change during the execution of the mission. This assumption provides a new strategy that consists in waiting at a vertex until an edge becomes traversable. It also transforms the problem into a Markov Decission Process that can be solved with the well known techniques of value and policy iteration.

In our case, as in [23], we assume a non-markovian graph where the state of the edges does not change once it is observed. In fact, the knowledge about the state of the environment is augmented as the graph is traversed and the future decisions are conditioned to this knowledge. In [23], the authors propose to expand the state of the formation (the nearest vertex where is placed) with the knowledge of the environment. With this approach they can assume that the expanded graph is markovian and thus they can prove that a convergent solution can be found. However, for practical issues, this approach is not optimal because the expanded graph has a number of vertices which is exponential in the number of edges in the original graph. Moreover, to apply the well known MDP solutions, the whole graph must be expanded.

The length of a path p can be expressed as a linear combination of the lengths of the edges of the graph, which can be expressed as a dot product. The coefficients are then the number of times each edge is included in the path. Thus, to find the shortest path we need to find the vector α_p that, representing a valid path, minimizes the dot product with L_E, the vector of the lengths of all the edges in the graph.

$$L(p) = \alpha_p^T \cdot L_E \tag{2}$$

In a deterministic framework, α_p is a binary vector (0 or 1-valued) indicating if an edge is included in the path or not. In the probabilistic framework considered in this paper, however, the coefficients are the expected number of times that each edge will be traversed while trying to reach the goal vertex using the shortest path. It is worth noting that in a probabilistic framework the expected number of times an edge is traversed can be bigger than 1, even if the initial path has no cycles. This is because at some point, the intended path may be non-traversable and thus the formation must go back to find an alternative path. Furthermore, there is a chance that in a probabilistic graph the goal is not reachable by any means from the starting vertex because some of the edges are in fact non-traversable. Given R the probability of the goal to be reachable computed from the prior knowledge of the graph and setting a penalty value λ if the goal is not reached, the expected length of a path $EL(p)$ can be expressed as,

$$EL(p) = R\alpha_p^T \cdot L_E + (1 - R)\lambda \tag{3}$$

The reachability R does not depend on the path p because the paths do exhaust all the possibilities to reach the goal if the initial intention is not traversable. Thus, the probability for any path to reach the goal is the same given the initial and final vertices and, therefore, the term $(1 - R)\lambda$ of equation 3 is constant. This fact allows some simplifications when searching for the best path p^* to reach the goal, as shown in (4), such as avoiding the computation of the reachability R which is as costly as computing the expected length or setting the penalization value λ to any arbitrary value. Instead, a score function $V(p)$ is minimized.

$$\begin{aligned} p^* &= \arg\min_p\{EL(p)\} \\ &= \arg\min_p\{R\alpha_p^T \cdot L_E + (1 - R)\lambda\} \\ &= \arg\min_p\{R\alpha_p^T \cdot L_E\} = \arg\min_p\{V(p)\} \end{aligned} \tag{4}$$

Given a path $p = (v_0, v_1, \ldots, v_n)$ from the initial vertex to the goal and knowledge about the state of the graph G, the score $V(v_0, v_1, \ldots, v_n|G)$ to minimize by equation (4) is defined as follows.

$$\begin{aligned} &V(v_0, v_1, \ldots, v_n|G) = P(v_0, v_1)V_1 + (1 - P(v_0, v_1))V_0 \\ &V_1 = L(v_0, v_1) + V(v_1, \ldots, v_n|G, P(v_0, v_1) = 1) \\ &V_0 = \min_{p'}\{V(p'|G, P(v_0, v_1) = 0)\} \end{aligned} \tag{5}$$

V_1 represents the expected length of the path given that the first edge is traversable and then calls recursively to compute the score of the rest of the path with the knowledge that the first link is traversable ($P(v_0, v_1) = 1$). This line of recursion finishes when the goal is reached since the score at the goal is 0.

$$V(v_n|\cdots) = 0$$

V_0, instead, represents the expected length of the best alternative path p' from v_0 to v_n given that the first edge is not traversable ($P(v_0, v_1) = 0$). In this case, the recursion finds a dead end when the non traversable edges block all the paths to the goal making it unreachable. The score for that situations is $V_0 = 0$ (λ in the general case).

The implementation of the score V of a path is shown in Algorithm 1.

Algorithm 1 Score of a path with memoization

```
def score(path, graph):
  if (path, graph) in memo:
    return memo(path, graph)
  if size(path) == 1: #at goal
    s = 0
  else:
    u = path[0]
    v = path[1]
    goal = path[n]
    prob = P(u,v)
    len = L(u,v)
    open = g ⋃ P(u,v) = 1
    os = len + score(p[1:], open)
    closed = g ⋃ P(u,v) = 0
    cs = min_score(u, goal, closed)
    s = prob * os + (1-prob) * cs
  memo(path, graph) = s
  return s

def min_score(start, goal, graph):
  paths = all_paths(start, goal, graph)
  if size(paths) == 0:
    return λ
  return min(score(path, graph)
                  for path in paths)
```

This solution implicitly explores, by recursion, the expanded graph mentioned above. However, there is no need to explore the whole expanded graph but only the nodes that are reachable from the initial conditions. Moreover, by keeping intermediate results (called *memoization* [26]) and bounds of the length of the final path, some pruning techniques can be applied to reduce the number of nodes expanded.

Example.

In Fig. 2a we show a toy example of the expected length of a path. There are two options to go from vertex A to vertex C: going directly or through vertex B. Depending on the value of the probability $P(B, C)$, the best path to reach C is different. There exists a traversable direct path $A \rightarrow C$ with a length of 30 units. However, if the edge BC is traversable, then there is a path to C through B with a length of 18 units. To know the state (open/closed) of the edge BC the node B must be first reached. The problem in moving to B first is that, in case the edge BC is not traversable, the formation has to go back to A to reach C, moving along the edge AB twice and thus making this path 32 units, thus longer than using directly the A $\rightarrow$ C path. Then, if the probability of BC being traversable is high enough ($P(B, C) > 0.727$), then it is worth moving first to vertex B because it is highly probable to find a path to C shorter than the direct path $A \rightarrow C$. Otherwise, if the edge BC is likely to be non-traversable, it is better to go directly to the goal. The graph in Fig. 2b shows the boundary point in the probability of being traversable for edge BC where the minimum expected length path changes. In Appendix A we present the developed computation of the EL of the two possible paths of this example.

It is proved that finding the minimum expected length path is an NP hard problem [23] and that the computational cost of the score algorithm grows exponentially with the number of vertices in the graph, as it considers every possible path and every possible knowledge of the graph. Also, graphs with high connectivity make the computation slower as the number of possible paths to evaluate grows. Then, in the following section, we propose a method to obtain a traversability map out of an a priori stochastic map which is simple enough to compute the expected length in a reasonable time while keeping the traversability information of the original map.

4. Global Traversability Map

To define the global traversability map we need a set of vertices and the corresponding edges among them with the corresponding length and traversability probability values. Let a stochastic feature-based representation (e.g., built by a SLAM algorithm), maybe partial and incomplete, either of the navigation area or of the local cooperative perception of the members of the robot formation, be represented by a set of geometric features $\mathbf{y}_{\mathcal{F}} = \{\mathbf{y}_{F_1}, \mathbf{y}_{F_2}, ..., \mathbf{y}_{F_N}\}$ known wrt a certain reference frame (not superscripted for simplicity). We obtain a

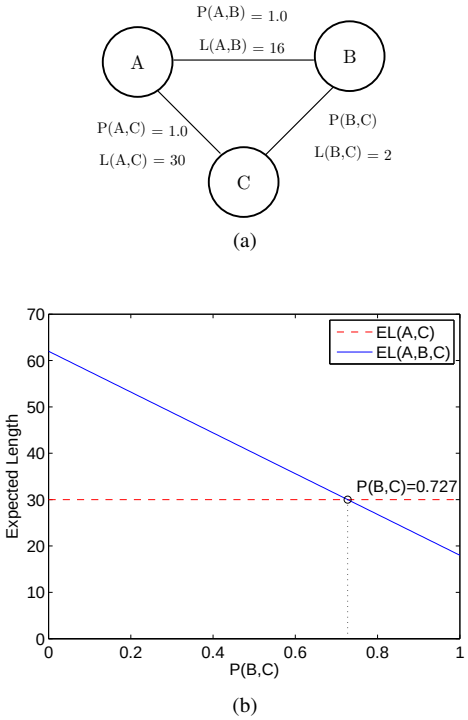

Figure 2: Example of expected path length algorithm. The best path from A to C depends on the probability $P(B,C)$. The boundary point, where the minimum expected length path changes, is at $P(B,C) = 0.727$. In this case, we assume $\lambda = 0$

probabilistic graph by applying the sample based technique presented in [27].

Fig. 3 shows an example of the application of this technique to obtain a traversability map from a feature-based stochastic map of an office-like environment. We also depict the collection of optimal paths for each of the map samples. Note the sharp edges at the bottom left part of the figure and blurred edges at the top right due to the greater uncertainty with respect to the base reference frame providing higher variability in the samples. The length and probability labels of the edges are detailed in section 6.1 with the results on global path planning.

5. Cooperative Replanning

In wide-opened and uncluttered environments once a global minimum expected length path for the robot leader is obtained, the robot followers would execute their paths, from origin v_0 to destination v_n, thanks to the links derived from the virtual spring-damper analogy of the robot formation and its commanded geometrical shape. However, in real settings frequent real-time replanning is mandatory to avoid unmapped or dynamic objects in the environment while flexibly and adaptively

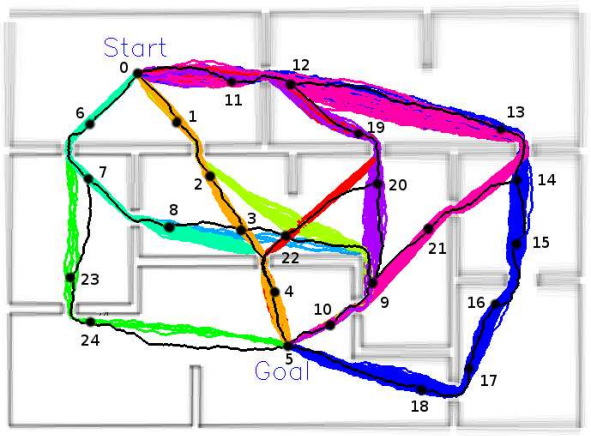

Figure 3: Stochastic map of the environment and the probabilistic graph obtained to compute a global path from the start (vertex 0) and the goal (vertex 5). The coloured lines are the clustered paths used during the construction of the graph.

maintaining the formation structure. Therefore, local safe paths for the robot formation must be computed frequently based on their common understanding of the environment and a sufficiently precise localization of the robots.

5.1. Pose Tracking of the Robot Formation

From an EKF-based perspective, a prediction of the stochastic discrete-time robot formation joint state vector $\mathbf{x}_{\mathcal{R}_k}$ and its covariance matrix $\mathbf{P}_{\mathcal{R}_k}$ can be computed from the linearization of eq. (1) as,

$$\begin{aligned} \mathbf{x}_{\mathcal{R}_{k|k-1}} &\simeq \mathbf{J}_{k-1}\mathbf{x}_{\mathcal{R}_{k-1}} + \mathbf{v}_{k-1} \\ \mathbf{P}_{\mathcal{R}_{k|k-1}} &\simeq \mathbf{J}_{k-1}\mathbf{P}_{\mathcal{R}_{k-1}}\mathbf{J}_{k-1}^T + \mathbf{Q}_{k-1} \end{aligned} \tag{6}$$

where the block-diagonal matrix $\mathbf{J}_{k-1}$ represents the Jacobian matrix of the linearized motion equations of the robot team, accurate for small rotations of the vehicles between time steps.

During navigation within the stochastic map, the robot formation obtains independent sets of observations from the environment at consecutive time instants, e.g., $\mathcal{E}_{k-1}$ and $\mathcal{E}_k$, that are matched against map features, e.g., $\mathcal{F}_{k-1}$ and $\mathcal{F}_k$ respectively, improving the estimated localization of the vehicles. Given that both $\mathcal{F}_{k-1}$ and $\mathcal{F}_k$ are subsets of features of the stochastic map, and therefore a cross-covariance term $\mathbf{P}_{\mathcal{F}_{k-1}\mathcal{F}_k}$ links together the constraints on the robot formation localization at time instants $k-1$ and k, a colored measurement noise scheme should be considered, otherwise, as reported in the preliminary results of [10], the white-noise assumption would drive the estimation out of consistency. Following the seminal work of [28] and the current practi-

cal approaches [29, 30, 31, 32] regarding the extension of the EKF-algorithm to colored measurement noise settings, the *measurement differencing* technique, that provides an efficient and mathematically sound method to remove the time-correlated portion of the measurement errors is considered.

At time step k, robust data association provides the algorithm with a set of jointly consistent pairs $(\mathbf{y}_{\mathcal{F}_k}, \mathbf{y}_{\mathcal{E}_k})$ of map features and sensor observations related by a linearized measurement equation of the form,

$$\mathbf{z}_k \simeq \mathbf{H}_k \mathbf{x}_k + \mathbf{G}_{\mathcal{F}_k} \mathbf{y}_{\mathcal{F}_k} \tag{7}$$

where $\mathbf{x}_k^T = \left(\mathbf{x}_{\mathcal{R}_k}^T, \mathbf{y}_{\mathcal{E}_k}^T\right)$ is an augmented state vector comprising the joint robot formation state and observations with $\mathbf{P}_k = \text{blkdiag}(\mathbf{P}_{\mathcal{R}_k}, \mathbf{P}_{\mathcal{E}_k})$ its joint covariance matrix, and $\mathbf{H}_k = (\mathbf{H}_{\mathcal{R}_k}\ \mathbf{H}_{\mathcal{E}_k})$ and $\mathbf{G}_{\mathcal{F}_k}$ are the Jacobian matrices of the linearized measurement equations with respect to the state vector $\mathbf{x}_k$ and the matched features $\mathbf{y}_{\mathcal{F}_k}$ respectively.

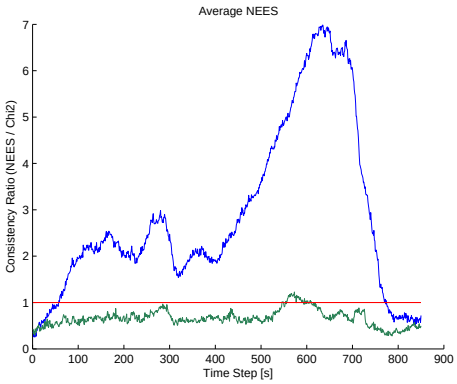

Figure 4: Consistency ratio (Normalized Estimation Error Squared / χ^2 threshold) comparison between the white-noise implementation of the EKF Update (blue) and the implementation based on the measurement differencing technique (green). The theoretical upper bound for the consistency ratio is equal to one. The average result of 10 Monte Carlo runs is depicted. Notice the localization still shows slightly inconsistent (i.e., ratio > 1) for a short period around timestep 600 due to a rotation performed by the formation, a high nonlinear situation.

The nature of the colored measurement noise driving eq. (7) is modeled by the linear transformation (also known as shaping or reduced-order filter) relating the two zero-mean jointly Gaussian random variables $\mathbf{y}_{\mathcal{F}_{k-1}}$ and $\mathbf{y}_{\mathcal{F}_k}$ (i.e., matched map features at time instants $k-1$ and k respectively) formulated as,

$$\mathbf{y}_{\mathcal{F}_k} = \mathbf{\Phi}_{C_k} \mathbf{y}_{\mathcal{F}_{k-1}} + \mathbf{n}_k \tag{8}$$

where,

$$\mathbf{\Phi}_{C_k} = \mathbf{P}_{\mathcal{F}_k \mathcal{F}_{k-1}} \mathbf{P}_{\mathcal{F}_{k-1}}^{-1} \tag{9}$$

and $\mathbf{n}_k$ is assumed to be a zero-mean white noise measurement sequence with covariance matrix,

$$\mathbf{P}_{\mathbf{n}_k} = \mathbf{P}_{\mathcal{F}_k} - \mathbf{P}_{\mathcal{F}_k \mathcal{F}_{k-1}} \mathbf{P}_{\mathcal{F}_{k-1}}^{-1} \mathbf{P}_{\mathcal{F}_{k-1} \mathcal{F}_k} \tag{10}$$

Thus, the measurement differencing technique obtains a whitened measurement equation from the weighted difference of colored measurement equations (in the form of eq. 7) at two consecutive time instants,

$$\mathbf{r}_k \triangleq \mathbf{z}_k - \mathbf{\Lambda}_k \mathbf{z}_{k-1} \simeq \mathbf{H}_k^* \mathbf{x}_k + \mathbf{w}_k \tag{11}$$

where matrix $\mathbf{\Lambda}_k$ is chosen such that the $\mathbf{r}_k$ is driven by the white-noise $\mathbf{w}_k$ only (Appendix B).

Being the colored noise setting a singular problem within the framework of Kalman-Bucy theory [33], the well-known EKF-update equations provide estimates for the augmented state vector $\mathbf{x}_k$ and its associated covariance matrix $\mathbf{P}_k$ using the pseudo-measurement eq. (11). Fig. 4 illustrates the consistency improvement provided by the measurement differencing implementation of the EKF-update step with respect to its white-noise implementation for a simulated experiment, with known data association, where a three-robot triangular-shaped formation is commanded to navigate along a 100m. loop trajectory in a previously mapped environment. Note that in the non-linear filtering context, the consistency cannot be *guaranteed* due to the linearization errors, therefore, efforts in the literature are oriented to lessen this problem (e.g., confer [34, 21]) as is the purpose of the proposed algorithm in this paper. A deeper study on this consistency issue in the context of multi-robot EKF localization and how it is also affected by an increasing number of robots can be found in [35].

5.2. Cooperative Local Planning

The performance (e.g., precision, reliability and robustness) of the robot formation to complete the commanded task profits from the close cooperation among the different vehicles of the team, emphasizing the importance of a centralized approach (at least at selected synchronization time steps) to consistently and coherently joint the views of the different vehicles.

Of paramount importance is the availability of this jointly coherent understanding of the navigation environment, with wider and integrated fields of views, to increase the efficiency and optimality of the on-line replanning process. For example, as illustrated in the experimental section, the best available path towards the next waypoint may be hidden to the robot leader (due to its limited sensorial field of view) but visible to one

of the followers, thus profiting the performance of robot formation replanning.

Since the robots in the formation navigate nearby, a number of redundant observations of the environment are found within the augmented state vector $\mathbf{x}_k^T = \left(\mathbf{x}_{\mathcal{R}_k}^T, \mathbf{y}_{\mathcal{E}_k}^T\right)$ estimated by pose tracking in the previous section. Therefore, geometrical constraints arise between features observed by different robots. Let $\mathbf{y}_{E_l}^{R_i}$ and $\mathbf{y}_{E_m}^{R_j}$ be two observations of the same map feature from robot R_i and R_j respectively. We can formulate a zero constraint (i.e., expressing the fact that the distance between both observations must be zero) as in eq. (12), where $\oplus$ and $\ominus$ are the operators that represent the direct and inverse transformation between reference frames, respectively.

$$\mathbf{h}(\mathbf{x}_{E_m}^{E_l}) = \ominus \mathbf{y}_{E_l}^{R_i} \ominus \mathbf{x}_{R_i}^{R_0} \oplus \mathbf{x}_{R_j}^{R_0} \oplus \mathbf{y}_{E_m}^{R_j} = \mathbf{0} \qquad (12)$$

These statistically joint consistent matches, from the Mahalanobis distance perspective, subsequently constraint the augmented state vector $\mathbf{x}_k$ in an EKF-update step, where the linearization of eq. (12) is used, resulting in a reduced, reliable, lower-uncertainty set of integrated sensor observations $\mathbf{y}'_{\mathcal{E}_k}$, characterizing the common understanding of the formation environment but also including all the unmatched observations.

Subsequently, a local traversability map Γ_{R_0} in the reference frame of the robot leader (thus leader-centric) obtained from the set of integrated observations $\mathbf{y}'_{\mathcal{E}_k}$ is required to compute a local path. The technique to obtain the traversability map proposed in section 4 cannot be applied in this case because the local traversability map presents a very simple topological structure which is not informative enough to be used by a local path planner.

Instead, we build the local traversability map out of this feature-based representation by projecting the features into a 2D regular lattice graph where the vertices are placed in the plane with a constant separation in both dimensions. Each vertex is connected only with its four immediate neighbors. Thus, the length of all the edges in the traversability map is constant $L(u, v) = \delta, \quad \forall (u, v) \in E$. The probability, for each edge of the graph, of being traversable is computed as the probability that no feature is projected in the space between the two vertices connected.

$$P(u, v) \triangleq \qquad (13)$$
$$1 - \text{Prob}\left(\bigcup_{n=1}^{N} \mathbf{y'}_{\mathcal{E}_n} \text{ is projected between } u \text{ and } v\right)$$

Real time constraints refrain from the exact computation of the probability values given by eq. (13) even for medium-scale environments. Thus, a sample-based method similar to the one used for building the global path is applied. However, instead of computing the best deterministic path for each sample of the stochastic set of observations $\mathbf{y}'_{\mathcal{E}_k}$, we accumulate all the samples into one graph. Then, for each edge, the probability of being traversable is defined as the proportion of samples in which the edge is not traversed by any feature. As example of this procedure, Fig. 5 shows the projection of two segments of a stochastic map.

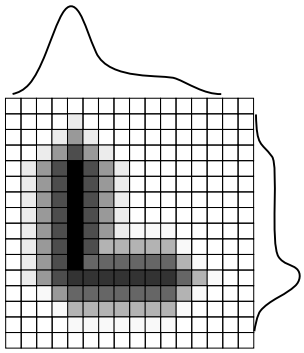

Figure 5: Sample traversability map obtained as the projection of a stochastic segment-based representation into a grid-based representation. The marginal probability density functions of two features (top and right) are shown together with the associated gray-scaled traversability values. The lighter the cell is, the higher the traversability probability between vertices. The marginal probability of finding an obstacle is also depicted at the top and the right side.

As mentioned in section 3, computing the path of minimum EL requires a high computational effort that cannot be achieved at the required frequency for a traversavility map like the grid obtained with the projection of the features. Instead, an A* path planning technique over the grid is applied to find the best path to the next waypoint. The cost function for the A* algorithm, the weighted length (WL), is computed so that it computes the very same best path that we would obtain using the minimum EL algorithm.

Thus, we define WL by weighting the length of the edges in the path p with the coefficients $\hat{\alpha}_p$, which are an approximation of the coefficients α_p in equation (2).

$$WL(p) = \hat{\alpha}_p^T \cdot L_E \qquad (14)$$

$$\hat{\alpha}_p^{(u,v)} = \begin{cases} \frac{1}{P(u,v)} & \text{if } (u, v) \in p \\ 0 & \text{if } (u, v) \notin p \end{cases} \forall (u, v) \in E \qquad (15)$$

As we can see in equation (16), the minimum WL criterion is a valid substitute of the minimum EL method when the probabilities in the traversability map are either close to 0 or to 1. In the local traversability maps,

which are built from the features currently observed by the formation, the uncertainties are of the order of the sensor accuracy. In other words, the state of the edges is known with a high confidence level. This fact implies that, in eq. (5), one of the terms $P(v_0, v_1)$ or $1 - P(v_0, v_1)$ will be close to 0, simplifying the computation. If all the edges are very likely to be traversable, then the expected length and the weighted length of the path are close to the total length of the path. On the other hand, if it is very likely for an edge to be non-traversable $P(v_0, v_1) \sim 0$, then the EL of a path traversing this edge is, in fact, the length of an alternative path. In addition WL will tend to infinity as $P(v_0, v_1)$ tends to 0, and thus, an alternative path will be chosen.

$$p^* = \arg\min_p \{EL(p)\} = \arg\min_p \{WL(p)\} \qquad (16)$$
$$\text{if } P(u, w) \to 0 \text{ or } P(u, w) \to 1,\ \forall (u, w) \in E$$

To illustrate this assertion, Fig. 6 shows the comparison of the expected and the weighted lengths in the example graph presented in Fig. 2a. In this example, all the probabilities are set to 1.0 except for $P(B, C)$. The figure shows that for $P(B, C) < 0.1$, the preferred path is $A \to C$ using both criteria. When $P(B, C) > 0.727$, the path $A \to B \to C$ minimizes the EL and the WL. When the probability is not that close to 0 or 1, then the results obtained from the two different criteria might disagree.

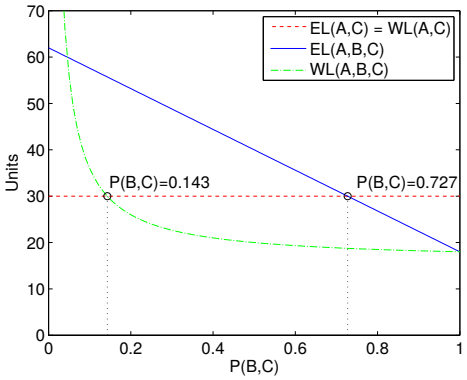

Figure 6: Expected length and weighted length for the two possible paths from vertex A to C in the example graph in Fig. 2a for different values of $P(B, C)$. Note that when the probability P(B,C) is close to 0 the path $A \to C$ presents the minimum expected length and weighted length. On the other hand, when P(B,C) tends to 1, the path $A \to B \to C$ minimizes the expected and the weighted lengths.

In addition to the local planning, to allow the formation replanning the global path so as to give more reactivity to the formation, all the waypoints of the global path not yet visited are considered as potential goals for the local path planner. The formation selects the waypoint that is closer in terms of WL, allowing some of the waypoints not to be visited if there is a shortcut in the global path. As exploration is not desired during the mission, local path planning is not allowed to search for paths that traverses unobserved zones. Section 6 shows simulated and real situations where the formation uses replanning for shortcutting the global path.

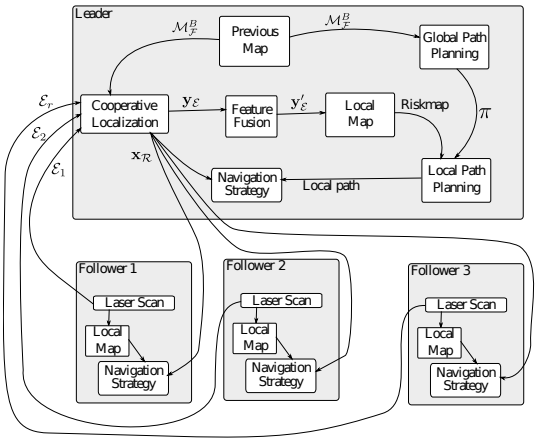

Figure 7: Overview of the hybrid centralized-distributed architecture of the reported integrated system. The schema depicts modules, relations and data flows, and execution threads (gray-shaded boxes). Data shared between different robots require the use of a communication protocol.

5.3. Cooperative Navigation

Fig. 7 depicts the hybrid centralized-distributed architecture of our integrated system with indication of the different modules, data flows and execution threads. Centralized execution refers to the robot leader thread whilst distributed execution refers to the robot followers threads.

Additionally, Algorithm 2 presents the procedures executed by the robot leader and the robot followers. The *leaderNavigationStrategy* and *moveLeader* functions track the local safe path that minimizes WL (eq. 14) thanks to the control strategy described in section 2. Furthermore, functions *followerNavigationStrategy* and *moveFollower* compute, distributively, the motion command for each robot follower in the formation. These two functions are directly adapted from the *strategy selection* and the leader and follower strategies defined by [20]. Three different navigation strategies are defined depending on the elements surrounding, as shown in Figure 8 .

Algorithm 2 Leader and Followers Algorithms

procedure LEADER($\mathbf{x}_{R_0,t_0}, \mathbf{x}_{R_0,t_f}, \mathcal{M}_{\mathcal{F}}^{\mathcal{B}}$)
  $\pi \leftarrow computeGlobalPath(\mathbf{x}_{R_0,t_0}, \mathbf{x}_{R_0,t_f}, \mathcal{M}_{\mathcal{F}}^{\mathcal{B}})$
  while last waypoint of π not reached **do**
    $\mathcal{E} \leftarrow gatherObservationsFromRobots(R_1, ..., R_r)$
    $\langle \mathbf{x}_{\mathcal{R}}, \mathbf{y}_{\mathcal{E}} \rangle \leftarrow poseTracking(\mathcal{E})$
    $\mathbf{y}'_{\mathcal{E}} \leftarrow cooperativePerception(\mathbf{y}_{\mathcal{E}})$
    $\Gamma \leftarrow buildLocalTraversabilityMap(\mathbf{y}'_{\mathcal{E}})$
    $sendInfoToFollowers(\mathbf{x}_{\mathcal{R}})$
    $\pi_{local} \leftarrow computeLocalPath(\Gamma, \pi)$
    $S_{leader} \leftarrow leaderNavigationStrategy(\mathbf{x}_{\mathcal{R}}, \pi_{local})$
    $moveLeader(S_{leader})$
  end while
end procedure

procedure FOLLOWER(R_0, R_i)
  while R_0 keeps moving **do**
    $\mathcal{E}_i \leftarrow gatherObservationsFromSensors(R_i)$
    $sendObservationsToLeader(\mathcal{E}_i)$
    $\mathbf{x}_{\mathcal{R}} \leftarrow getLocFromLeader(R_0)$
    $S_{follower_i} \leftarrow followerNavigationStrategy(\mathbf{x}_{\mathcal{R}}, \mathcal{E}_i)$
    $moveFollower(S_{follower_i})$
  end while
end procedure

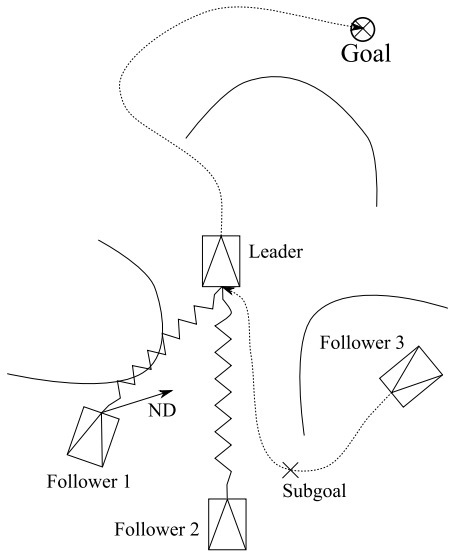

Figure 8: Navigation strategies for the followers. Follower 1 uses formation control with obstacle avoidance (Nearness Diagram), follower 2 uses only formation control and follower 3 temporarily uses a single robot path planning strategy to avoid a complex obstacle.

The stability issues of the formation technique based on spring-damper analogy were addressed more deeply in previous papers, [20] and [22]. The set of navigation strategies guarantees that the formation converges to the stable configuration in open environments. The obstacles temporarily push the formation out of the desired shape, but the use of the correct strategy in each situation moves the robots back to their predefined position when the obstacles are avoided.

In very complex environments with cluttered obstacles, the robots switch to a single robot navigation strategy, relaxing the formation constraints to avoid any blocking situation. As soon as the complexity of the environment decreases, the formation constraints are recovered and the robots converges back to the desired configuration.

6. Experimental Results

In this section we report both simulated and real experiments obtained by a formation in the presence of sensing, localization and mapping uncertainties as described along the previous sections. We first illustrate, from a simulation-based perspective (Player-Stage simulation environment): (i) the computation of global and local optimal plans; (ii) the adaptability of the geometric structure of the robot formation to the dynamics of the environment; and (iii) the benefits of cooperative perception in replanning tasks. Then, in a real setting, we show the performance of the complete integration scheme in a navigation task commanded to a three-robot formation in an indoor scenario.

6.1. Global Path Planning

In this section, we will use the stochastic map of the office-like environment depicted in Fig. 3 to illustrate the procedure to compute the minimum expected length global path.

This map was constructed previously to the navigation execution and has been enriched with a topological probabilistic graph, using the technique proposed in section 4. Table 1 shows the corresponding lengths and probabilities of the edges in this traversability map.

In Table 2 we show the evaluation of a subset of the paths from the start (vertex 0) to the goal (vertex 5) using different methods. The TL column is the total length of the path assuming that all the edges are always traversable. The P column shows the probability for a path to be traversable. The fourth column shows the weighted distance WL of the path. This is the cost function used in the cooperative local replanning (see equation 14). Finally, the last column shows the evaluation of the paths according to their expected length computed using the algorithm in Fig. 1.

The shortest path is the path C (TL), however it is the path with lowest probability of success (P). On the

Table 1: Distances (L) and probabilities (P) of the edges in the traversability graph depicted in Fig. 3.

EDGE	P	L	EDGE	P	L
(0, 1)	1.00	3.87	(9, 10)	0.97	3.82
(0, 6)	1.00	4.16	(9, 20)	1.00	6.48
(0, 11)	1.00	6.12	(9, 21)	1.00	4.77
(1, 2)	0.46	4.14	(9, 22)	1.00	7.38
(2, 3)	1.00	3.89	(11, 12)	0.99	3.98
(3, 4)	0.57	4.49	(12, 13)	1.00	13.55
(3, 8)	1.00	4.73	(12, 19)	1.00	5.17
(3, 22)	1.00	2.77	(13, 14)	0.99	4.31
(4, 5)	1.00	3.51	(14, 15)	1.00	4.06
(4, 22)	0.57	4.20	(14, 21)	0.91	6.36
(5, 10)	1.00	2.97	(15, 16)	1.00	4.92
(5, 18)	1.00	9.03	(16, 17)	1.00	4.33
(5, 24)	1.00	12.71	(17, 18)	1.00	4.36
(6, 7)	0.53	4.69	(19, 20)	0.77	3.86
(7, 8)	1.00	6.05	(20, 22)	1.00	6.66
(7, 23)	1.00	6.44	(23, 24)	0.89	3.81

contrary, the path G presents the highest probability of success but it is longest one. The minimum expected length path (EL) is the path E and, the path with minimum weighted length (WL), which is the approximation of the EL we use for local planning, is the path C. This is due to the fact that WL is not considering the real penalty of finding an alternative path in a graph which is not very dense and where the uncertainty of traversability is very high for some edges. So, the EL approach represents the adequate cost to be applied in global path planning.

Concerning computation time, finding the minimum expected length path for this case took 4 minutes long on a Intel Core^{TM} i7-3770 computer, which is reasonable for an offline global path planning task.

Additionally, we have analyzed the sensitivity of the minimum EL path to variations in the probabilities of the edges computed using the method proposed in 4. We run different monte-carlo simulations with truncated normal distributions with mean the estimated probabilities shown in Table 1 and with different standard deviations. The use of different probability values changes the expected length of the paths. However, as shown in Table 3, with standard deviations up to 0.01 the best path remains the same as using their initial estimation. With larger values of σ, some replications result in a different best path $(0, 1, 2, 3, 4, 5)$, which has an expected length very close to the optimal $(0, 11, 12, 19, 20, 9, 10, 5)$ as shown in Table 2. Thus, it is shown that changes in the estimation of the probabilities do not affect to the resulting minimum expected length path up to a reasonable limit.

6.2. Formation Adaptability

Fig. 9 shows a typical office-like indoor environment where a five-robot formation is commanded to navigate from an initial location (labeled *Start*) towards a final destination (labeled *Goal*). Thanks to the robot formation integrated control scheme, the robots compliantly maintained the user-defined geometric structure (pentagon-shape in this case) along the way.

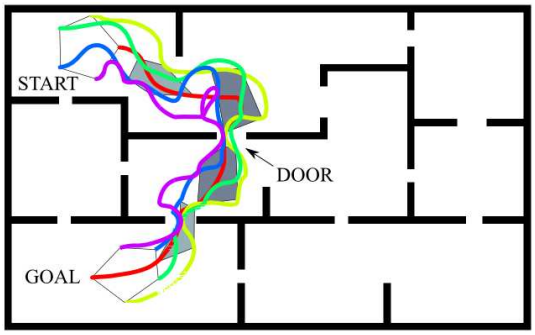

Figure 9: Five-robot formation adaptability to a simulated indoor environments. From the individual traces of the different vehicles we observed that they compliantly maintained the user-defined geometric structure (pentagon-shape in this case) whilst navigating through narrow and wide open spaces towards the commanded goal destination.

The system computes the safest global path (in the traversability map associated to the navigation area) between the start and the goal locations that is dynamically updated by cooperative replanning thanks to the different observations of the individual vehicles. Note that vehicles align to traverse the different doors whilst they tend towards the commanded geometric shape in wide-open areas. It is also remarkable that, even with very narrow zones where robot have to wait for others to navigate through doors, the formation never gets stuck thanks to the use of the different navigation strategies.

6.3. Cooperative Replanning

Fig. 10 reports the behavior of the five-robot formation in an open-door event detected by one of the robot followers and transmitted to the robot leader thanks to the cooperative perception strategy reported above. Initially, the global path planning algorithm drives the robot formation from the initial location to the final location (Figs. 9 and 10a) through the way-point $\mathbf{x}_{G_1}$. Then, while navigating towards $\mathbf{x}_{G_1}$ a shortest path to the goal destination appears when the labeled door (Fig.

Table 2: Comparison of different criteria to choose the best global path.

	Path	TL	P	WL	EL
A:	(0, 6, 7, 23, 24, 5)	31.82	0.47	37.45	43.60
B:	(0, 6, 7, 8, 3, 4, 5)	27.64	0.30	36.18	44.32
C:	(0, 1, 2, 3, 4, 5)	**19.90**	0.26	**29.15**	39.23
D:	(0, 11, 12, 19, 20, 22, 4, 5)	33.52	0.43	38.88	45.92
E:	(0, 11, 12, 19, 20, 9, 10, 5)	32.40	0.74	34.71	**38.97**
F:	(0, 11, 12, 13, 14, 21, 9, 10, 5)	45.87	0.87	47.70	47.17
G:	(0, 11, 12, 13, 14, 15, 16, 17, 18, 5)	54.67	**0.98**	55.75	54.61

Table 3: Sensitivity of the minimum expected length path for different standard deviations of the probabilities of the edges.

Std. dev. (σ)	% unchanged best path
0.01	100%
0.025	99.9%
0.1	70.8%
0.25	53.6%

9) becomes wide open but, unfortunately, this event occurs outside the field of view of the robot leader. Nevertheless, cooperative replanning, thanks to the common understanding of the navigation area (Fig. 10b) allows the correction of the previously planned path profiting the robot formation from the short-cut to the goal.

Note that the replanning to the new waypoint is possible because the new path traverses observed zones.

A video with the complete execution of this simulation is available [1].

6.4. Localization consistency

Regarding the localization, we have measured the consistency of the algorithm proposed in section 5.1 in terms of the NEES which, compared to a chi-square distribution, provides a statistical test to assess the filter consistency. Fig. 11 shows the consistency ratio NEES/$\chi^2_{r,1-\alpha}$ ($r = \dim(\mathbf{x}_{\mathcal{R}_k})$ degrees of freedom with significance level $\alpha = 0.05$). Most of the time, the consistency is under the required threshold. The maximum near $t = 50$ is produced by the fact that the formation is entering in a big room where their range-limited sensors are not able to find as many features as in other rooms in the scenario. Furthermore, at certain points during the execution of this simulation (see trajectory in Fig. 9) the formation has to reorganize itself to head to the next subgoal and to adapt its shape to the environment constraints, involving high rotations on the robots, which, as explained in Sec. 5.1, introduce high non-linear errors in the estimation affecting slightly and for short pe-

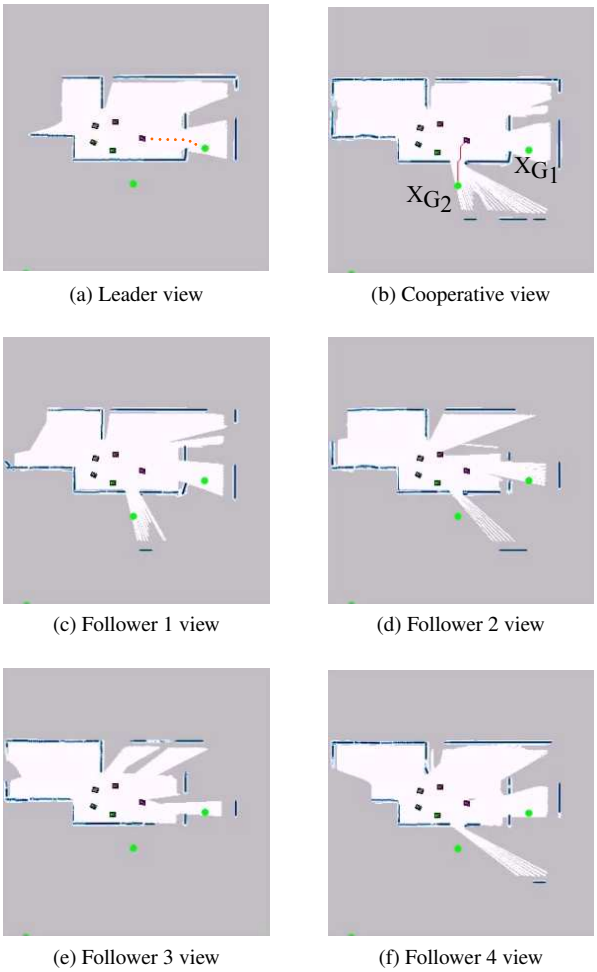

(a) Leader view (b) Cooperative view

(c) Follower 1 view (d) Follower 2 view

(e) Follower 3 view (f) Follower 4 view

Figure 10: Cooperative replanning towards the goal destination $\mathbf{x}_{G_2}$. The figure shows the integrated field of view in the reference frame of the leader (10b) and the different individual perspective of each robot in the formation. Fig. 10a shows the erroneous path planned from the perspective of the robot leader in the absence of cooperation with other team members.

[1] http://webdiis.unizar.es/u/urcola/videos/5-robots.avi

riods the consistency. However, the algorithm is able to recover from this situation and the estimation remains consistent during the most part of the simulation.

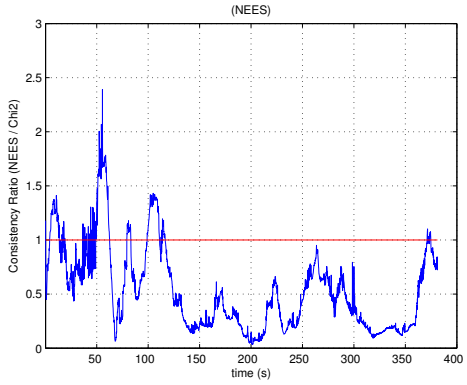

Figure 11: Consistency ratio NEES/$\chi^2_{r,1-\alpha}$ obtained in the simulation using the measurement differencing based EKF implementation. Consistency is achieved when the ratio is ≤ 1.

6.5. *Experiments in Real Scenarios*

Through the real experiments we want to test the different aspects of the proposed system, such as cooperative localization and navigation of the robot formation and global path planning and cooperative replanning under uncertainty. However, it is not easy to find a challenging scenario to test all these aspects simultaneously. Instead, we make use of two different scenarios to: (i) test the global path planner given a stochastic map of a real environment and (ii) test the on-line performance of the proposed system and how the formation copes with changes in the environment. We have experimented with a three-robot Pioneer 3-AT formation equipped with on-wheel encoders and SICK LMS-200 laser rangefinders with a 180-deg field of view. Communication between the vehicles is achieved by a dedicated channel using a real time wireless multi-hop protocol [36], which includes communication queues to avoid synchronization failures.

The hybrid centralized-distributed implementation of the complete system reported computation times of the order of the laser scan cycle (approx. 4.5 Hz) where a maximum of 100 samples have been used to compute the traversability maps during cooperative replanning. Table 4 shows the divergence and consistency measurements for different number of samples. The values for 100 samples are clearly better than the ones obtained for 10 samples but the improvement in using 1000 samples is very small. Thus, using 100 samples seems to be a good compromise between acceptable approximation and computation costs.

Table 4: Results of the analysis of the sample size. KL-divergence is the median of the divergences measured in nats and consistency is the percentage of consistent sampling

Samples	10	100	1000
KL-divergence	46.51	34.71	33.65
Consistency	53.64	98.38	99.86

In the first experiment we test the global path planner in the medium-size office-like environment depicted in Fig. 12. Using the Monte Carlo technique explained in section 4 we extract the traversability graph from the stochastic map of the environment whose edges are labeled according to Table 5.

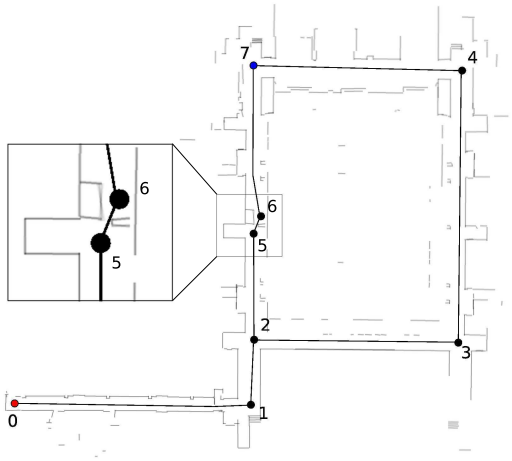

Figure 12: Global path planning. The algorithm favors the longer but more probable path against the shortest path due to the high uncertainty area on the middle of the corridor (detail enlarged on the left of the figure).

Table 5: Distances (m) and probabilities corresponding to the traversability graph of the real experiment depicted in Fig. 12.

Edge(u, v)	P(u, v)	L(u, v)
$(0, 1)$	1.0	33.8
$(1, 2)$	1.0	9.6
$(2, 3)$	1.0	29.3
$(2, 5)$	1.0	15.45
$(3, 4)$	1.0	39.3
$(4, 7)$	1.0	29.1
$(5, 6)$	0.1	3.1
$(6, 7)$	1.0	20.8

The global path planner have been executed to compute the minimum expected length path from the initial

location of the robot formation (vertex 0) towards the final destination (vertex 7). The algorithm selects the path $(0, 1, 2, 3, 4, 7)$ as the one with minimum expected length (EL = 141.1 m) in contrast to the shorter but less probable path $(0, 1, 2, 5, 6, 7)$ with an expected length of 163.075 m. This shorter path passes through an area with high risk of being non traversable (see partial map enlarged on the left of the figure) due to the presence of clutter in the corridor. The probability of this area being traversable is encoded in $\text{EDGE}(5, 6)$. The boundary point for this value is $P(5, 6) = 0.346$. If it were higher, the shortest path would have been chosen.

Global replanning. In case the selected path is found non-traversable, i.e., the box is actually blocking the corridor, the formation must replan a new global path to the goal. Using the information computed during the initial path planning, which is kept thanks to memoization, the formation can select the optimal path with the current state of knowledge (the corridor with the box is non-traversable).

In the second experiment, we address the problem of the cooperative localization, perception, navigation and replanning in a changing environment. As illustrated in Fig. 13 and Fig. 14, a three-robot triangular-shaped formation is commanded to navigate from $\mathbf{x}_{G_1}$ towards $\mathbf{x}_{G_5}$. During the map building process, the door labeled in the figure was closed and this has been reflected in the a priori stochastic map provided to the formation. Consequently, the global planner computes a path from $\mathbf{x}_{G_1}$ towards $\mathbf{x}_{G_5}$ via the sequence of ordered waypoints shown in the figure.

During the mission execution, this door, outside of the robot leader's field of view, is opened and observed by the robot followers, therefore the reported cooperative strategy replans the path towards the goal destination skipping the waypoints $\mathbf{x}_{G_3}$ and $\mathbf{x}_{G_4}$. This video [2] shows the complete execution of the mission in which the real-time capabilities of the reported strategy and the adaptability of the formation to the new scenario are demonstrated.

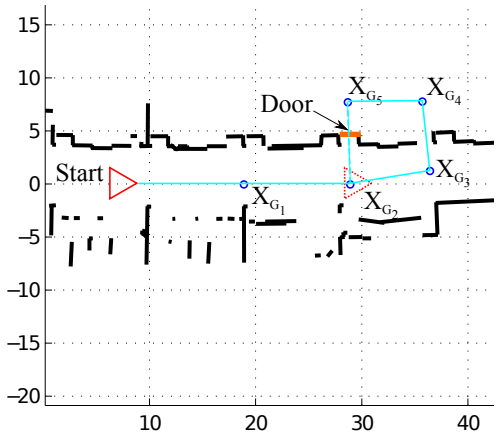

Figure 13: Cooperative replanning scenario. A three-robot triangular-shaped formation (solid red) is commanded from $\mathbf{x}_{G_1}$ towards $\mathbf{x}_{G_5}$ via the sequence of ordered waypoints (solid blue line). During the execution, a door (labeled) outside of the field of view of the robot leader is opened and observed by the robot followers (dotted red triangle), therefore the reported cooperative strategy replans the path towards the goal destination (dashed blue line) skipping the waypoints $\mathbf{x}_{G_3}$ and $\mathbf{x}_{G_4}$.

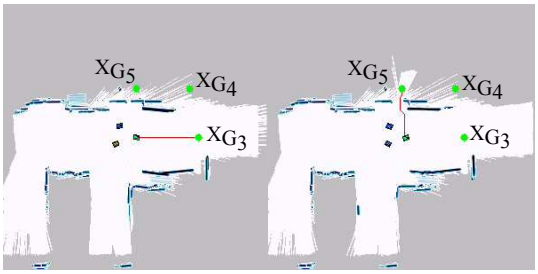

(a) Planning towards X_{G_3}. (b) Planning towards X_{G_5}.

(c) Moving along the corridor. (d) Heading to the opened door.

Figure 14: Cooperative replanning. The leader is able to replan a better path through the opened door thanks to the observations of the other robots in the formation.

7. Conclusions

This paper has reported an tightly integrated real-time system for robot formations in the presence of sensing, localization and mapping uncertainties. A expected length of global paths for the robot leader is minimized, which considers the probability of choosing a way in which the robots have to come back in the event of finding non traversable zones whilst navigating, leading to longer paths. The selected way is tracked by the formation thanks to a cooperative sensor-based replanning technique that dynamically adapts the robot formation structure to the complexity or changes of the environ-

[2] `http://webdiis.unizar.es/u/urcola/videos/ada-byron.avi`

ment whilst avoiding obstacles. Accurate pose tracking of the robot formation has been achieved by a mathematically sound strategy that paired sensor observations with map features building consistent maps derived from a previously known stochastic model of the navigation area. Experimental results, both in simulation and in realistic medium-size office-like settings, have illustrated the performance of the described approach by using a hybrid, centralized-distributed, architecture with wireless communication capabilities achieving a 4.5 Hz cycle-time for a three-robot triangular-shaped formation.

As future work, a deeper analysis of the minimum expected length algorithm would improve its performance, which grows exponentially with the number of edges in the graph. Its potential extension to other scenarios in which the density of obstacles or people can change depending on the time or along the days (i.e., traffic flows, hospitals, offices...) is also being considered, where the expected length will depend on that density. Future work should search for further distributed approaches, thus reducing the frequency of synchronization among the vehicles and increasing the modularity of the system, but maintaining the accuracy and real-time decision making capabilities of the reported hybrid approach. Also, occasional interruptions in the communications between the robot followers and the robot leader should be considered together with the mathematical sound treatment of out-of-sequence interactions.

Finally, regarding formation control, it would be interesting as well to let the robots change the role inside the formation so as to minimize the forced maneuvers when sudden changes of goals occur.

Acknowledgment

This work was partially supported by the Spanish project DGA-FSE (T04) and the MINECO-FEDER projects DPI2012-36070 and DPI2012-32100.

Appendix A. Developed example for expected length computation

In Fig. A.15, we develop the score computation of the two alternative paths in the toy example shown in Fig. 2a using Algorithm 1.

Appendix B. Derivation of the pseudo-measurement equation for pose tracking

To avoid time latency, we rearrange eq. (6) following [31] as,

$$\mathbf{x}_{\mathcal{R}_{k-1}} \simeq \mathbf{J}_{k-1}^{-1}\mathbf{x}_{\mathcal{R}_k} - \mathbf{J}_{k-1}^{-1}\mathbf{v}_{k-1} \tag{B.1}$$

Substituting eqs. (7), (8) and (B.1) into eq. (11) we obtain,

$$\mathbf{r}_k \simeq \mathbf{H}_k^*\mathbf{x}_k + \mathbf{w}_k \tag{B.2}$$

where

$$\mathbf{H}_k^* = \begin{pmatrix} \mathbf{H}_{\mathcal{R}_k} - \mathbf{\Lambda}_k\mathbf{H}_{\mathcal{R}_{k-1}}\mathbf{F}_{k-1}^{-1} & , \mathbf{H}_{\mathcal{E}_k} \end{pmatrix} \tag{B.3}$$

and the white noise sequence $\mathbf{w}_k$, with covariance matrix $\mathbf{P}_{\mathbf{w}_k}$, is given by,

$$\mathbf{w}_k = \mathbf{\Lambda}_k\mathbf{H}_{\mathcal{R}_{k-1}}\mathbf{F}_{k-1}^{-1}\mathbf{v}_{k-1} - \mathbf{\Lambda}_k\mathbf{H}_{\mathcal{E}_{k-1}}\mathbf{y}_{\mathcal{E}_{k-1}} + \mathbf{G}_{\mathcal{F}_k}\mathbf{n}_k \tag{B.4}$$

and,

$$\mathbf{\Lambda}_k = \mathbf{G}_k\mathbf{F}_{C_k}\mathbf{G}_{\mathcal{F}_{k-1}}^T(\mathbf{G}_{\mathcal{F}_{k-1}}\mathbf{G}_{\mathcal{F}_{k-1}}^T)^{-1} \tag{B.5}$$

which cancels out the dependency of $\mathbf{r}_k$ on $\mathbf{y}_{\mathcal{F}_{k-1}}$ (see [28] for the original derivation).

Then, the EKF update equations provide estimates for the augmented state vector $\mathbf{x}_k$ and its associated covariance matrix $\mathbf{P}_k$ in the colored noise setting using the filter gain given by,

$$\begin{aligned} \mathbf{K}_k &\triangleq \mathbf{P}_{\mathbf{x}_k\mathbf{r}_k}\mathbf{P}_{\mathbf{r}_k}^{-1} \\ &= (\mathbf{P}_{k|k-1}\mathbf{H}_k^{*T} + \mathbf{C}_k)\cdot \\ &\quad (\mathbf{H}_k^*\mathbf{P}_{k|k-1}\mathbf{H}_k^{*T} + \mathbf{P}_{\mathbf{w}_k} + \mathbf{H}_k^*\mathbf{C}_k + \mathbf{C}_k^T\mathbf{H}_k^{*T})^{-1} \end{aligned} \tag{B.6}$$

with $\mathbf{P}_{k|k-1}$ the predicted covariance matrix,

$$\mathbf{P}_{k|k-1} = \text{blkdiag}\left(\mathbf{F}_{k-1}\mathbf{P}_{\mathcal{R}_{k-1}}\mathbf{F}_{k-1}^T + \mathbf{Q}_{k-1}, \mathbf{P}_{\mathcal{E}_k}\right)$$

and $\mathbf{C}_k$, the correlation term between $\mathbf{v}_{k-1}$ and $\mathbf{w}_k$ due to the constraint imposed by eq. (B.4), completed with zeros to fit the dimensions of $\mathbf{H}_k^*$,

$$\mathbf{C}_k = E[\mathbf{v}_{k-1}\mathbf{w}_k^T] = \mathbf{Q}_{k-1}(\mathbf{\Lambda}_k\mathbf{H}_{\mathcal{R}_{k-1}}\mathbf{F}_{k-1}^{-1})^T$$

[1] R. W. Beard, J. Lawton, F. Y. Hadaegh, A coordination architecture for spacecraft formation control, IEEE Trans. on Control Systems Technology (2001) 777–790.

[2] E. Z. MacArthur, C. D. Crane, Compliant formation control of a multi-vehicle system, in: Proc. IEEE International Symposium on Computational Intelligence in Robotics and Automation, 2007, pp. 479–484.

[3] P. Urcola, L. Riazuelo, M. T. Lázaro, L. Montano, Cooperative navigation using environment compliant robot formations, in: IEEE/RSJ Int. Conf. on Intelligent Robots and Systems, Nice, France, 2008, pp. 2789–2794.

[4] M. A. Lewis, K.-H. Tan, High precision formation control of mobile robots using virtual structures, Auton. Robots 4 (4) (1997) 387–403.

$$
\begin{aligned}
V(A \to C) &= P(A,C)(L(A,C) + \overbrace{V(C|AC)}^{0}) + (1 - \overbrace{P(A,C)}^{1})V(A \to B \to C|\overline{AC}) = 30 \\
V(A \to B \to C) &= P(A,B)(L(A,B) + V(B \to C|AB)) + (1 - P(A,B))V(A \to C|\overline{AB}) \\
&= 16 + P(B,C)(L(B,C) + V(C|AB,BC)) + (1 - P(B,C))V(B \to A \to C|AB,\overline{BC}) \\
&= 16 + 2P(B,C) + (1 - P(B,C))(L(B,A) + V(A \to C|AB,\overline{BC})) \\
&= 16 + 2P(B,C) + (1 - P(B,C))(16 + P(A,C)(L(A,C) + V(C|AB,\overline{BC},AC)) + (1 - P(A,C))\lambda) \\
&= 16 + 2P(B,C) + (1 - P(B,C))(16 + 30) = 62 - 44P(B,C)
\end{aligned}
$$

Figure A.15: Score computation of the two alternative paths in the toy example shown in Fig. 2a. The notation XY means that the edge (X, Y) is known to be traversable while $\overline{XY}$ means that the edge is non-traversable. Figure 2b shows the graph of the scores of the two alternatives depending on the probability $P(B, C)$.

[5] J. V. Gómez, A. Lumbier, S. Garrido, L. Moreno, Planning robot formations with fast marching square including uncertainty conditions, Robotics and Autonomous Systems 61 (2) (2013) 137 – 152.

[6] R. Kurazume, S. Nagata, S. Hirose, Cooperative positioning with multiple robots, in: IEEE Int. Conf. on Robotics and Automation, Los Alamitos, CA, 1994, pp. 1250–1257.

[7] I. M. Rekleitis, G. Dudek, E. Milios, Multi-robot exploration of an unknown environment, efficiently reducing the odometry error, in: Fifteenth International Joint Conference on Artificial Intelligence, Nagoya, Japan, 1997, pp. 1340–1345.

[8] A. C. Sanderson, A distributed algorithm for cooperative navigation among multiple mobile robots, Advanced Robotics 12 (4) (1998) 335–349.

[9] W. Burgard, D. Fox, D. Hennig, T. Schmidt, Estimating the absolute position of a mobile robot using position probability grids, in: Proc. of the Fourteenth National Conference on Artificial Intelligence (AAAI-96), 1996, pp. 896–901.

[10] M. T. Lázaro, J. A. Castellanos, Localization of probabilistic robot formations in SLAM, in: IEEE Int. Conf. on Robotics and Automation, Anchorage, Alaska, 2010, pp. 3179–3184.

[11] D. Fox, W. Burgard, H. Kruppa, S. Thrun, A probabilistic approach to collaborative multi-robot localization, Autonomous Robots 8 (2000) 325–344.

[12] S. I. Roumeliotis, G. A. Bekey, Distributed multi-robot localization, IEEE Trans. on Robotics and Automation 18 (5) (2002) 781–795.

[13] A. Martinelli, F. Pont, R. Siegwart, Multi-robot localization using relative observations, in: IEEE Int. Conf. on Robotics and Automation, Barcelona, Spain, 2005, pp. 2808–2813.

[14] D. Ferguson, M. Likhachev, A. Stentz, A guide to heuristic-based path planning, in: Proc. of the International Workshop on Planning under Uncertainty for Autonomous Systems, International Conference on Automated Planning and Scheduling (ICAPS), 2005.

[15] H. Kurniawati, T. Bandyopadhyay, N. M. Patrikalakis, Global motion planning under uncertain motion, sensing, and environment map, Autonomous Robots 33 (2012) 255–272.

[16] J. V. D. Berg, P. Abbeel, K. Goldberg, LQG-MP: Optimized path planning for robots with motion uncertainty and imperfect state information, The International Journal of Robotics Research 30 (7) (2011) 895–913.

[17] R. He, S. Prentice, N. Roy, Planning in information space for a quadrotor helicopter in a GPS-denied environment, in: IEEE Int. Conf. on Robotics and Automation, Pasadena, CA, 2008, pp. 1814–1820.

[18] A. J. Briggs, C. Detweiler, D. Scharstein, A. Vanderberg-Rodes, Expected shortest paths for landmark-based robot navigation, The International Journal of Robotics Research 23 (7–8) (2004) 717–728.

[19] R. Valencia, M. Morta, J. Andrade-Cetto, J. M. Porta, Planning reliable paths with pose slam, IEEE Transactions on Robotics 29 (4) (2013) 1050–1059.

[20] P. Urcola, L. Montano, Cooperative robot team navigation strategies based on an environmental model, in: IEEE/RSJ Int. Conf. on Intelligent Robots and Systems, St. Louis, MO, 2009, pp. 4577–4583.

[21] J. A. Castellanos, R. Martinez-Cantin, J. D. Tardós, J. Neira, Robocentric map joining: Improving the consistency of EKF-SLAM, Robotics and Autonomous Systems 55 (1) (2007) 21–29.

[22] J. R. Asensio, L. Montano, A kinematic and dynamic model-based motion controller for mobile robots, in: 15th IFAC World Congress on Automatic Control, Barcelona, Spain, 2002.

[23] G. H. Polychronopoulos, J. N. Tsitsiklis, Stochastic shortest path problems with recourse, Networks 27 (1996) 133–143.

[24] E. Nikolova, D. R. Karger, Route planning under uncertainty: The canadian traveller problem, in: The Twenty-Third AAAI Conference on Artificial Intelligence, Vol. 2, 2008, pp. 969–974.

[25] C. Papadimitriou, M. Yannakakis, Shortest paths without a map, Theoretical Computer Science 84 (1991) 127–150.

[26] D. Michie, "memo" functions and machine learning, Nature 218 (1968) 1922.

[27] P. Urcola, M. T. Lazaro, J. A. Castellanos, L. Montano, Generation of probabilistic graphs for path planning from stochastic maps, in: European Conference on Mobile Robots, 2015, pp. 1–7.

[28] A. E. Bryson, L. J. Henrikson, Estimation using sampled data containing sequentially correlated noise, Journal of Spacecraft and Rockets 5 (6) (1968) 662–665.

[29] P. Tortora, Y. Oshman, F. Santoni, Attitude independent estimation of spacecraft angular rate using geomagnetic field observations, in: IEEE Aerospace Conference, 2003, pp. 2637–2645.

[30] M. Joerger, B. Pervan, Autonomous ground vehicle navigation using integrated GPS and laser-scanner measurements, in: IEEE/ION Position, Location, and Navigation Symposium, 2006, pp. 988–997.

[31] M. G. Petovello, K. O'Keefe, G. Lachapelle, M. E. Cannon, Consideration of time-correlated errors in a Kalman filter applicable to GNSS, Journal of Geodesy 83 (2009) 51–56.

[32] K. Wang, Y. Li, C. Rizos, Practical approaches to kalman fil-

tering with time-correlated measurement errors, IEEE Trans. on Aerospace and Electronics Systems 48 (2) (2012) 1669–1681.

[33] A. E. Bryson, D. E. Johansen, Linear filtering for time-varying systems using measurements containing colored noise, IEEE Trans. on Automatic Control (1965) 4–10.

[34] T. Bailey, J. Nieto, J. Guivant, M. Stevens, E. Nebot, Consistency of the EKF-SLAM algorithm, in: IEEE/RSJ Int. Conf. on Intelligent Robots and Systems, Beijing, China, 2006.

[35] M. T. Lázaro, Map building, localization and exploration for multi-robot systems, Ph.D. thesis, Universidad de Zaragoza (January 2015).

[36] D. Tardioli, J. L. Villarroel, Real time communications over 802.11: RT-WMP, in: Proc. IEEE International Conference on Mobile Adhoc and Sensor Systems MASS, Pisa, Italy, 2007, pp. 1–11. doi:10.1109/MOBHOC.2007.4428607.